HENRY

Hydraulic Engineering Repository

Ein Service der Bundesanstalt für Wasserbau

Conference Paper, Published Version

Grossmann, Florian; Gawehn, Matthijs; de Vries, Sierd; de Wit, Floris P.; Aarninkhof, Stefan G. J.

Comparison of Currents Derived from X-band Radar and Collected In-situ Data in Ameland Inlet

Comparison of Currents Derived from X-band Radar and Collected In-situ Data in Ameland Inlet

F. Grossmann
Delft University of Technology, Delft, Netherlands & Universitat Politècnica de Catalunya, Barcelona, Spain

M. Gawehn
Delft University of Technology, Delft, Netherlands & Deltares, Delft, Netherlands

S. de Vries
Delft University of Technology, Delft, Netherlands

F. P. de Wit
Delft University of Technology, Delft, Netherlands

S. G. J. Aarninkhof
Delft University of Technology, Delft, Netherlands

Abstract: Velocities derived from X-band radar were compared to depth-averaged ADCP measurements in a complex tidal inlet system at Ameland, the Netherlands. Observed differences between ADCP and radar were clustered and related to water level elevations, wind velocities, wave period, wave height, spatial coherence in radar output and error metrics of the fitting procedure. Larger waves and higher wind velocities were observed to benefit radar agreement with ADCP results. Rising water levels benefitted agreement in east-west direction. Falling water levels benefitted agreement in north-south direction. No correlation between observed differences and spatial coherence was observed. In the applied error metrics, only the east-west confidence interval showed a good correlation with observed differences. The radar at Ameland monitors the whole inlet system and provides current velocities everywhere in its range. This study shows that the radar's currents are in good agreement with ADCP depth-averaged currents throughout the tidal cycle. Furthermore, it stresses radar's potential for better monitoring of the coast and cost-effective coastal field measurements to obtain large datasets, even in hydrodynamically very complex regions.

Keywords: Remote Sensing, Coastal Field Measurements, Current Monitoring, Depth Inversion, X-Band Radar, SEAWAD, Kustgenese 2.0, XMFit

1 Introduction

The magnitude and direction of currents play an integral role in sediment dynamics and coastal morphology. To understand local morphodynamics, it is therefore valuable to measure currents. This can be done with in-situ or remote sensing techniques. In-situ measurements are costly due to the required man hours and equipment. Also, and despite their accuracy, common problems include the influence of carrying structures (Mueller, 2015) and the limited spatial coverage. Remotely-sensed current measurements are generally coarser than in-situ measurements but offer several advantages (Holman and Haller, 2013, Gangeskar, 2018): The equipment does not need to resist violent wave action in the surf zone; there is no danger to operators installing, repairing or retrieving equipment; and the equipment is not affected by scouring, burying or fouling. Moreover, remote sensing has the potential to provide measurements over larger areas at high temporal resolution and low cost.

In recent years, the interest for remote sensing in coastal engineering has been growing. Systems were developed to measure wave characteristics, wave dissipation, bathymetry and current vectors (Holman and Haller, 2013). A particular example, based on radar, is the X-band MATLAB® Fitting (XMFit) algorithm (Friedman, 2014). It was developed at TU Delft and Deltares and it is a 3D-Fourier based method as proposed by Young et al. (1985). It estimates both bathymetry and near-surface

currents. Currently, it is used to monitor the morphodynamics of the Ameland ebb-tidal delta in the Netherlands for the Dutch coastal research project Coastal Genesis 2.0 (Gawehn et al., 2019 *in prep.*).

In this paper we compare depth-averaged currents from in-situ measurements to XMFit currents. Subsequently, we cluster observed differences and relate them to environmental conditions, spatial coherence in radar output and error metrics of the fitting procedure to form a better understanding under which conditions radar provides reliable current velocities. To our knowledge, this is one of the first studies to conduct a detailed validation of radar with in-situ currents in a hydrodynamically very complex region like Ameland inlet.

2   Methodology

Results from a field campaign, conducted in September 2017, offered the opportunity to compare remote sensing-derived current estimates (from X-band radar) with in-situ data (from an Acoustic Doppler Current Profiler (ADCP) measurement frame) at the northern edge of Ameland inlet's ebb-shield (Fig. 1). In this study, environmental data, measured at nearby stations or estimated from numerical models, spatial coherence in the remote sensing method and error metrics are related to observed differences between ADCP and radar. September 2017 was characterized by a combination of calm conditions and storm events (notably storm Sebastian peaking on September 13th).
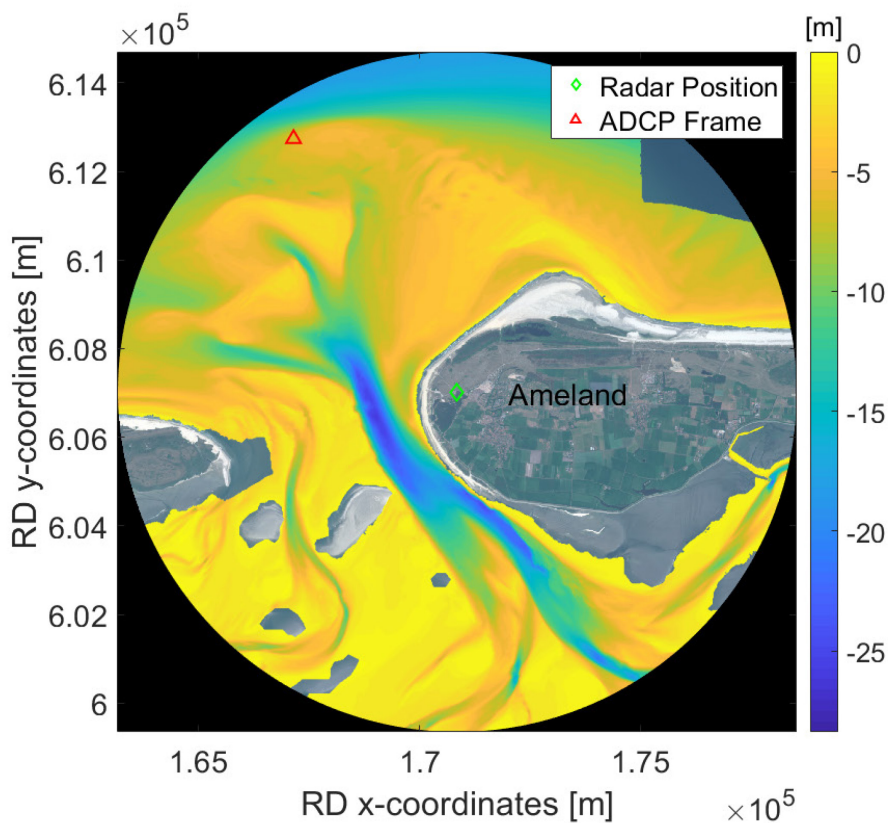

Fig. 1.   Satellite image of Ameland inlet georeferenced to Dutch Rijksdriehoekscoördinaten with image size corresponding to radar range. Depths superimposed from combined bathymetric surveys (February and September 2017) and indicated by colorbar on the right. Positions of radar (green diamond) and ADCP frame (red triangle) indicated by markers.

2.1   ADCP Measurements

To enable a comparison with radar, ADCP measurements are depth averaged. An upward-looking Teledyne RDI Workhorse Monitor ADCP gathered velocity data while a downward-looking Nortek Aquadopp Current Meter measured pressures. The sensors were mounted onto a stainless-steel frame and the frame was placed on the seabed. Under the assumption of hydrostatic pressure, the measured pressures are used to calculate the water surface elevation. The obtained information is used to delimit the ADCP's submerged bins and it is assumed that velocity is constant between uppermost bin and water surface. If at least three data points are available in the vertical profile, a Piecewise Cubic

Hermite Interpolating Polynomial is fitted to the data points between sensor location and a pre-defined point 0.48 m below the calculated water surface. The depth-integrated profile is then divided by the distance between ADCP and the pre-defined point to obtain the depth-averaged velocity components. The pre-defined point is set because the assumption of hydrostatic pressure does not allow accurate calculation of the water surface and waves are found to contaminate velocity estimates near the surface. Profiles are mostly logarithmic with small deviations in upper regions, arguably due to wind influence.

2.2 Radar Measurements

The radar used for data acquisition operates from the lighthouse at Ameland inlet. It has a range of 7.675 km but is cut off at 7.5 km in order to minimize the effect of inaccuracies at the boundary. The resolution of a single pixel is 7.5 m with one radar image containing 2048 such pixels. The framerate of the radar images is 2.85 s.

XMFit is based on the Doppler-shifted linear dispersion relationship. Radar images of backscatter intensity are divided into computational cubes and stacked in time. Via application of a 3D-FFT (Fast Fourier Transform) the energy spectrum $E(k_x, k_y, \omega)$ is obtained (Young et al., 1985). The image intensity dispersion shell in three-dimensional wavenumber-frequency space is then fitted to dispersion relationships. Depth and current information of the best-fitting theoretical dispersion shell is output. For more elaborate information on the theoretical basis of the algorithm refer to the work of Gawehn et al. (2019 *in prep.*).

Radar results for velocity correspond to a weighted depth-average (Stewart and Joy, 1974). In this study, a spatial domain of roughly 1 km^2 is used to obtain a single depth-averaged velocity which is then compared to the ADCP velocity measured at the frame. Like the ADCP velocities, radar velocities are time averaged over intervals of 12 minutes – the intervals will be referred to as epochs. In each epoch, calculations are made at the ADCP frame location and surrounding points (Fig. 2). Medians and means, of the velocities obtained in all calculation points, are used to select a single output velocity, representing the epoch. Even though XMFit can be run without depth input, the algorithm is run in depth-assimilated mode to constrain the solution. A combined bathymetry from single beam surveys in February and September 2017 is used as ground truth depth.
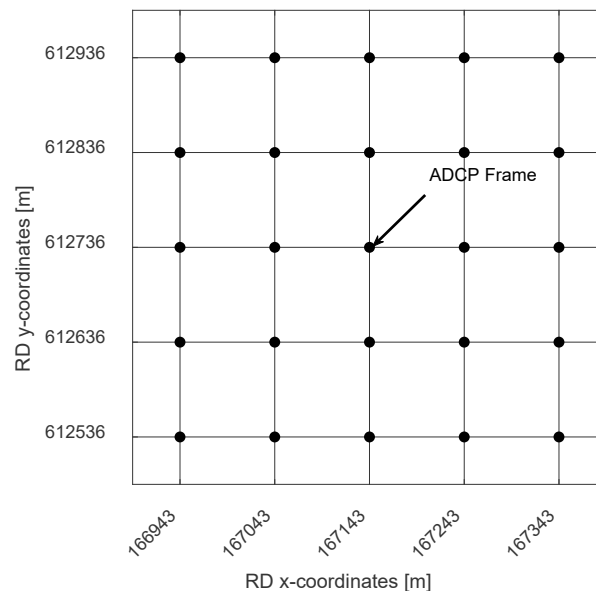
Fig. 2.   Schematization of calculation points (black circles) for calculation of radar velocities. Points surround the ADCP frame in steps of 100 m.

XMFit does not output velocities if the fitting procedure violates error metric settings (e.g. $R^2 < 0.6$). Medians and means are only calculated and output if velocities were output in five or more calculation points. Furthermore, the medians of the most important error metrics of all calculation points per epoch are calculated and saved. The error metrics include the Coefficient of Determination (R^2) and Root Mean Square Error (RMSE), representing the correlation between image intensity and

theoretical dispersion shells, as well as directional confidence intervals, representing the uniqueness with which XMFit's Levenberg Marquardt algorithm selects the output directional current component.

2.3 Environmental Measurements

Water level data is obtained from the tide gauge at Terschelling and from the pressure sensor on the ADCP frame. Wave parameters are obtained from Deltares's MATROOS visualization tool for Ameland Station 1-1. Wind data is obtained from station L91. For all environmental measurements, the stations, that represented conditions at the ADCP frame most accurately, are chosen. Data was retrieved in 1 h intervals corresponding to the end date of velocity-averaging epochs.

2.4 Comparison Procedure

ADCP and radar velocities are averaged over the same spatial and temporal domains (but note that averaging depth in radar varies depending on wavenumber (Stewart and Joy, 1974)). Comparison of output velocities per epoch yields the difference between ADCP and radar and allows the clustering of epochs according to difference characteristics. The comparison is conducted via the velocities' directional components in east-west and north-south.

The radar output velocity per epoch is selected as the mean or median over all calculation points per epoch. Error metrics, gauging the correlation of ADCP and radar velocities, are used to compare mean and median. The first metric is bias, representing the average difference between ADCP and radar output over the whole experiment. The second metric is the unbiased Root Mean Square Error (uRMSE), representing the correlation between ADCP and radar output corrected for bias.

The spatial coherence of an epoch describes how similar output velocities in the calculation points (Fig. 2) are. Differences between ADCP and radar and environmental measurements are compared to the observed spatial coherence. Subsequently, differences between ADCP and radar are compared to extrema in error metrics of the fitting procedure. Additionally, differences between ADCP and radar are compared to environmental measurements. For wave parameters and wind velocity, the influence of extrema on differences between ADCP and radar and on spatial coherence is observed. For water levels, the influence of phases in the tidal cycle on differences between ADCP and radar is observed.

3   Results and Discussion

Results for current velocity (from ADCP and radar), error metrics and environmental conditions are stated and analyzed in context with each another. Subsequently, the resulting implications on current estimation via radar are discussed.

3.1 Comparison of Currents

ADCP current measurements conform to expected southeastern and northwestern flow directions (Elias, 2017) in the study area (Fig. 3). The highest current magnitudes are observed in eastern direction. Radar-derived median estimates capture the changing directions throughout the tidal cycle except for some outliers. The radar median "correctly" represents maximum velocities in eastward direction but tends to overestimate westward directed velocities, compared with the ADCP. A northward bias is observed in northward direction and there is difficulty in estimating southward directed currents via radar. Epochs are clustered according to the relation of outputs.

Good epochs are defined to feature differences between ADCP and radar smaller than 0.1 m/s. The east-west component contains 27 good epochs and the north-south component 14 (Fig. 3). In the east-west component, consecutive good epochs are frequently visible, mostly at times of westward directed currents (e.g. Fig. 3; epochs 12 and 13, 22-25 and 55-57). In the north-south component, the tendency is more towards individual good epochs (e.g. Fig. 3; epochs 1, 49 and 60) but consecutive good epochs are also observed (e.g. Fig. 3; epochs 38-41, 69 and 70).

Bad epochs are defined to feature differences between ADCP and radar larger than 0.5 m/s. The east-west component contains 3 bad epochs and the north-south component 6 (Fig. 3). In the east-west component, they result from overestimation in westward direction (e.g. Fig. 3; epochs 29, 45 and 46).

In the north-south component, they are linked to the northward bias (e.g. Fig. 3; epochs 8, 19 and 20, 72 and 73 and 88). Under the margin of 0.5 m/s, a partly consecutive and partly individual character of bad epochs becomes visible but only few epochs are available. When lowering the boundary to 0.3 m/s to observe more bad epochs, a mainly consecutive character of 2-3 consecutive bad epochs dominates in the north-south component (14 bad epochs under 0.3 m/s margin) whereas the east-west component is dominated by individual bad epochs (14 bad epochs under 0.3 m/s margin).

Opposite direction epochs are defined to feature ADCP and radar indicating opposite directions. The east-west component contains 16 opposite direction epochs and the north-south component 37 (Fig. 3). In the east-west component, opposite direction epochs mainly occur individually in between the matching direction epochs. They either occur because of single fluctuations (e.g. Fig. 3; epochs 5, 26, 44, 46, 68 and 89), because the radar indicates a change of direction to the west earlier than the ADCP (e.g. Fig. 3; epochs 15, 22 and 37) or because the radar indicates a change of direction to the east later than the ADCP (e.g. Fig. 3; epochs 50, 61 and 62). In the north-south component, opposite direction epochs occur partly individually (e.g. Fig. 3; epochs 21, 57 and 89) and partly in subsequence to one another (e.g. Fig. 3; epochs 9-15, 31-37 and 74-79). They mainly occur because of the radar's northward bias and inability to follow the ADCP as current turns southward.
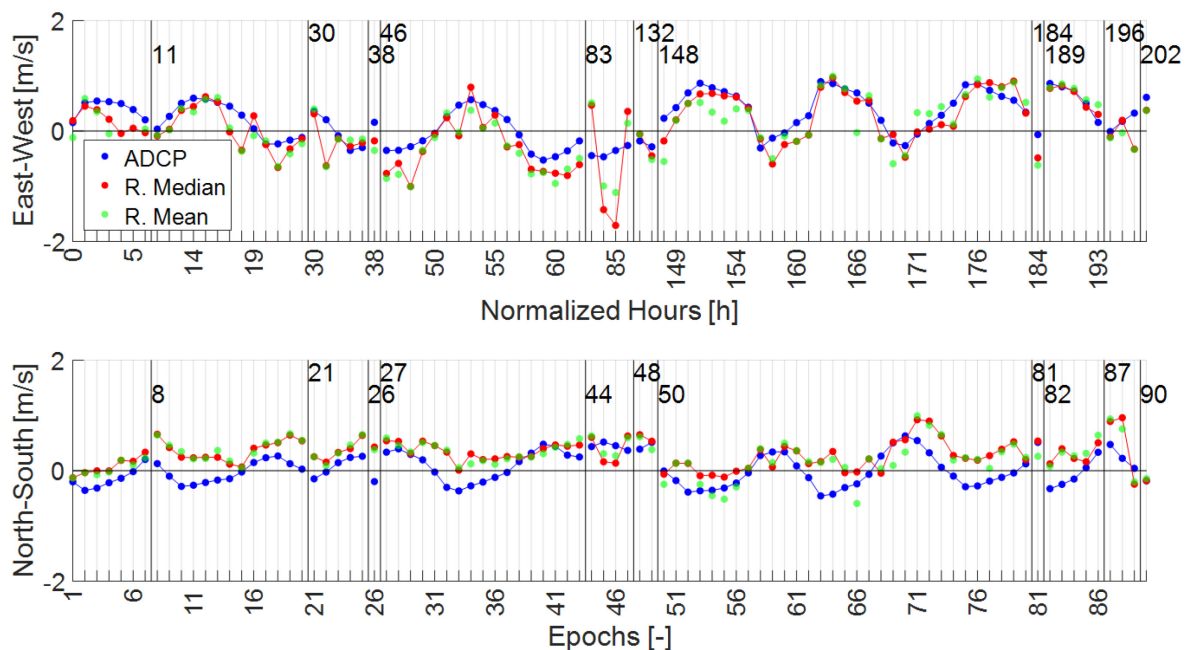

Fig. 3.   ADCP results (blue) in comparison with radar-derived median (red) and mean (green) estimates for the east-west (top) and north-south (bottom) velocity component. Flow to the east and north is defined positive and to the west and south is defined negative. Note that on the lower x-axis, epochs are shown in consecutive order up to data gaps (vertical black lines), resulting from quality control measures in radar and in-situ data processing as explained in section 2. The upper x-axis features the duration of the experiment in hours, normalized to the first epoch 31-Aug-2017 09:32:38 and capturing the size of the data gaps.

Overshoot epochs are defined to feature radar estimating the maximum positive or negative velocity component magnitudes of the tidal cycle higher than observed by the ADCP. The east west component contains 16 overshoot epochs and the north south component 14 (Fig. 3). In the east-west component, overshooting occurs in eastward direction at times but more frequently in westward direction (e.g. Fig. 3; epochs 18, 34 and 70). In the north-south component, there is a northward bias in many epochs and overshooting only occurs in northward direction (e.g. Fig. 3; epochs 18, 28 and 71). The tendency towards consecutive overshooting is stronger in the north-south component, where the northward bias shifts velocities above the ADCP measurement in consecutive epochs, than in the east-west component, where overshooting occurs more frequently but individually, apart from one group of consecutive epochs (e.g. Fig. 3; epochs 39-43).

Outlier epochs are, on the one hand, defined to feature surrounding epochs comparing well with the ADCP but single outlying epochs being subject to much larger differences between ADCP and radar (e.g. Fig. 3; epochs 18, 29 and 89 in the east-west component and epoch 59 in the north-south component). On the other hand, outlier epochs are defined to feature surrounding epochs showing a large difference between ADCP and radar but single epochs comparing very well with the ADCP (e.g.

Fig. 3; epoch 36 in the east-west component and epochs 15, 29, 69 and 70 in the north-south component). As the timestep between good and bad agreement is very short (roughly one hour), the sudden change in correlation is surprising. The east-west component contains 12 outlier epochs and the north-south component 7 (Fig. 3). Note that a small number of epochs are part of multiple clusters.

Tab. 1.   Clustered epochs shown component-wise and in percent of the total epochs in the experiment. Summation does not equal 100 % because certain clusters may overlap and not every epoch fulfills at least one of the clustering conditions.

	Good [%]	Bad [%]	Opposite [%]	Overshoot [%]	Outlier [%]
East-West	30	3.33	17.78	17.78	13.33
North-South	15.56	6.67	41.11	15.56	7.78

Current magnitude is obtained as the vector sum of the east-west and north-south current components. Vector summation is observed to distort single components' differences between ADCP and radar: When both components are within the good fit margin, magnitude is not necessarily "good" because small differences between ADCP and radar are magnified by the vector summation. If both components contain differences between ADCP and radar in the same direction (e.g. Fig. 3; epoch 1) or one component's difference is nearly as large as the margin (e.g. Fig. 3; epoch 80), magnitude is observed to be above the margin. Therefore, good agreement in current magnitude does not guarantee that directional components are "good". On the contrary, good agreement in current magnitude often results from an underestimation difference in one directional component, balanced by an overestimation difference in the other component and potentially involving estimation of opposite directions (e.g. Fig. 3; epochs 58 and 68). Therefore, we consider current magnitude only of secondary importance for the analysis.

3.2   Spatial Coherence and Error Metrics

The 25 velocity outputs that are calculated per epoch, are spaced in steps of 100 and 200 m around the ADCP location. This procedure is chosen because comparing multiple outputs provides a more resilient result. Furthermore, the analyzed domain is large (roughly 1 km^2) and representing it with a single output velocity seems doubtful. By shifting the calculation points by 100 and 200 m from the ADCP frame location, the conditions in the whole domain are represented more accurately. Additionally, the procedure produces less epochs without any output. Yet, spatial coherence of radar output is subject to variations (Fig. 4).
In addition to the median, the mean per epoch is shown in comparison to ADCP output (Fig. 3). The mean is often further from the ADCP result than the median (Tab. 2). This is attributed to faulty outliers that affect the result more strongly in the mean. Evidently, the choice of a representative output value affects the difference between radar and ADCP and there could be a more accurate statistical measure than the median.

Tab. 2.   Bias and uRMSE between radar median and ADCP and radar mean and ADCP. Output points spaced in steps of 100 m.

	Median, Bias	Mean, Bias	Median, uRMSE	Mean, uRMSE
Magnitude	0.2598	0.3900	0.3189	0.2975
East	-0.1664	-0.1948	0.3041	0.3107
North	0.2658	0.2314	0.2392	0.2626

Epochs of good spatial coherence coincide with epochs of large wave height and high wind magnitude (e.g. Fig.s 4, 7 and 8; epochs 51-54, 56-63 and 82-88). This indicates that high wind velocity and wave height benefit spatial coherence. Corresponding differences between ADCP and radar, on the other hand, are partly small and partly large so that no correlation between spatial coherence in output and differences can be identified. The east-west component is characterized by much worse spatial coherence than the north-south component even though it shows smaller differences than the north-south component (Fig.s 3 and 4). Furthermore, epochs of bad spatial coherence are observed to coincide both with small and large differences between ADCP and radar (e.g. Fig.s 3 and 4; epochs 47, 50, 55 and 66). The same applies to epochs of good spatial coherence (e.g. Fig.s 3 and 4; epochs 21-25 and 58-60).
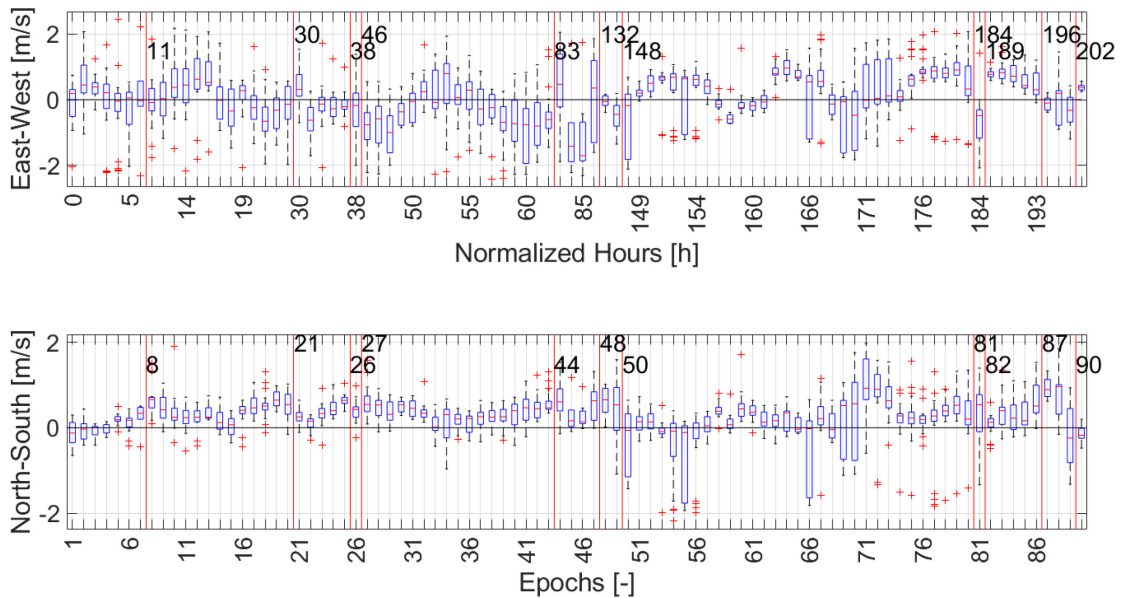
Fig. 4. Boxplot of east-west (top) and north-south (bottom) velocity components per epoch. Red horizontal line indicating median per epoch and boxes the 25th and 75th percentiles. Outliers represented by '+' symbol and defined as more than three scaled median absolute deviations. Whiskers representing the most extreme outputs not considered outliers. X-axes corresponding to Fig. 3. Good spatial coherence indicated by small boxes and small whiskers.

Epochs of large and small R^2 coincide with differences of varying size. Epochs with small and large RMSE also coincide with differences of varying size. Therefore, no correlation between differences and R^2 or RMSE is found.

In the confidence interval east-west, larger intervals are observed in most of the experiment's first half (e.g. Fig. 5; epochs 8-47). The epochs of large intervals are characterized by low waves and low wind magnitude (e.g. Fig.s 7 and 8; epochs 8-47). The corresponding differences between ADCP and radar in the east-west component frequently show substantial differences and outliers (e.g. Fig. 3; epochs 8-47). In the second half of the experiment, the differences between ADCP and radar in the east west component show differences and outliers less frequently and they are smaller (e.g. Fig. 3; epochs 48-90). In the first half of the north-south confidence interval (e.g. Fig. 5; epochs 8-47), the same wave heights and similarly low wind magnitudes apply (e.g. Fig.s 7 and 8; epochs 8-47). However, the size of the confidence intervals is limited to the smaller intervals in the east-west component and differences in confidence interval size between the first and the second half do not show as clearly (Fig. 5). In the north-south component, only limited correlation between confidence intervals and differences between ADCP and radar becomes visible (Fig.s 3 and 5).
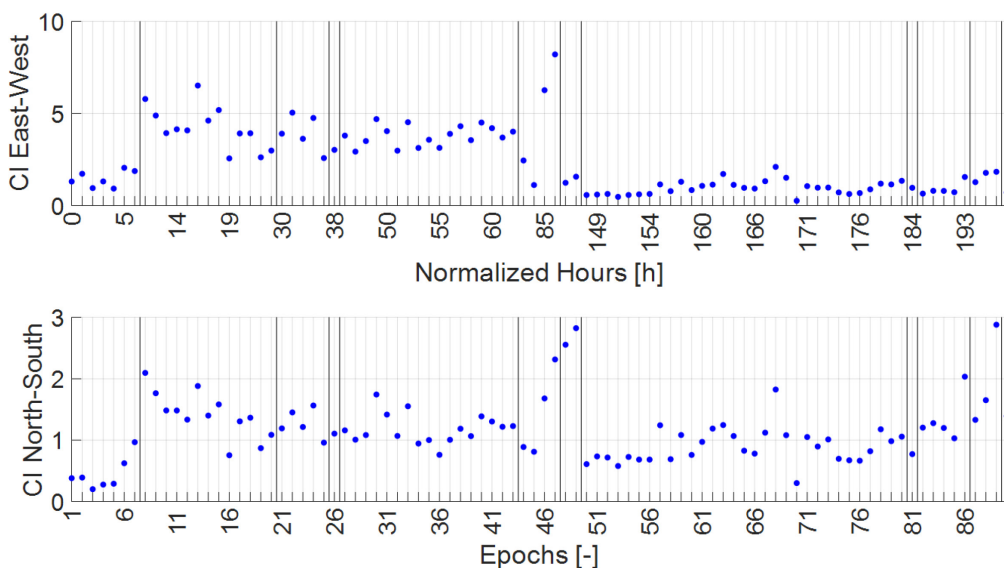

Fig. 5. Error metrics of radar fitting procedure averaged per epoch. High correlation indicated by high R^2 and low RMSE and confidence intervals. X-axes corresponding to Fig. 3.
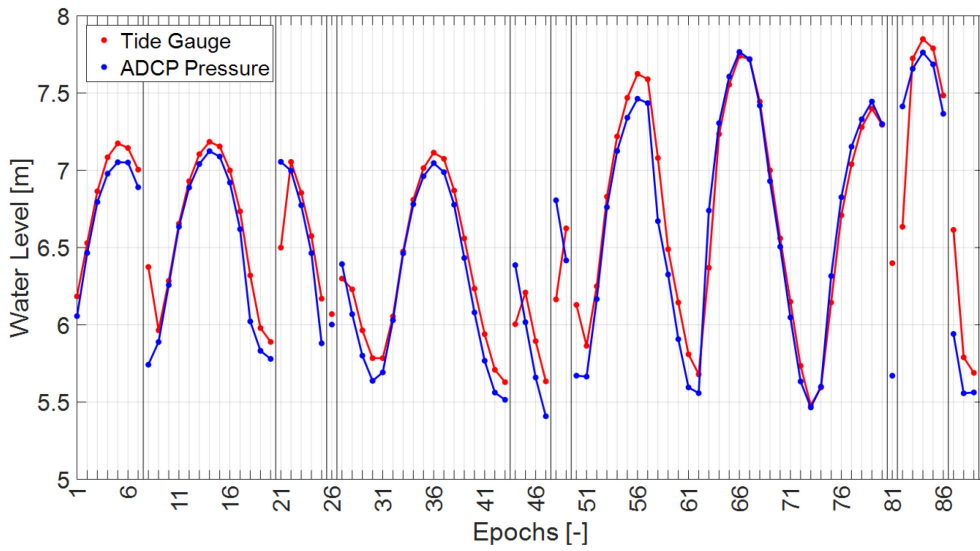
422

Fig. 6.   Water levels from tide gauge measurements (red) and pressure measurements at the ADCP frame (blue). X-axis corresponding to Fig. 3.
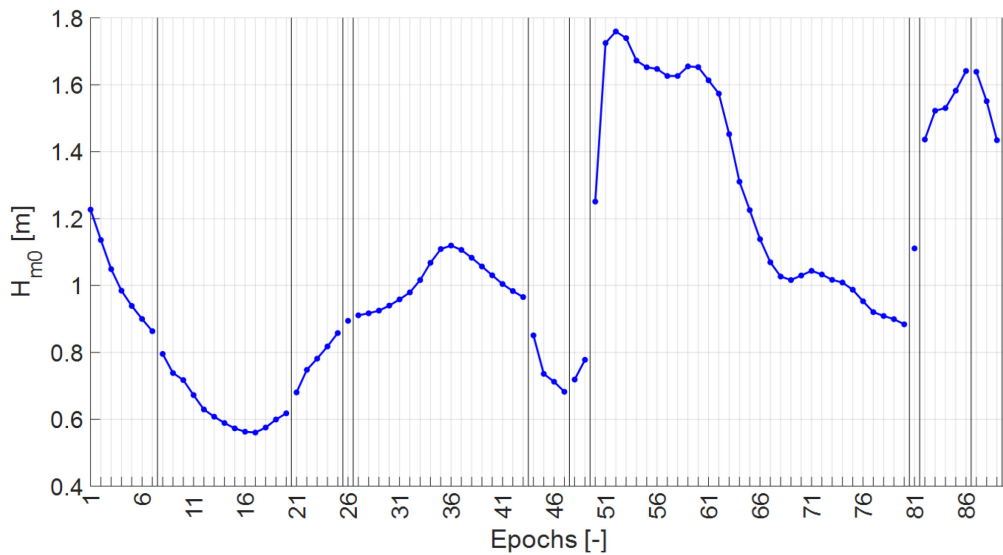

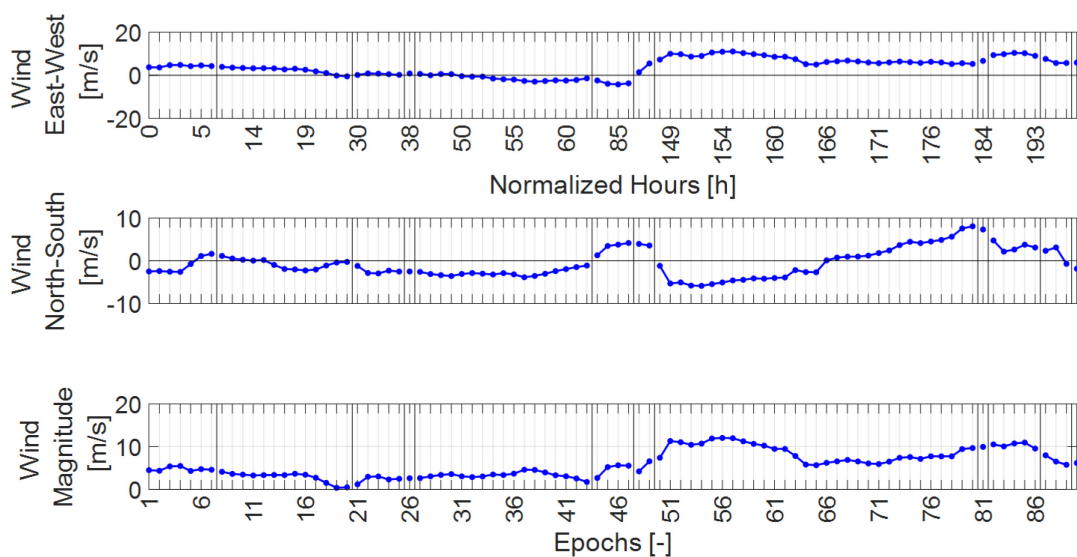Fig. 7.   Wave height H_{m0} (blue) with x-axis corresponding to Fig. 3.

Fig. 8.   Wind velocity east-west (top), north-south (middle) and magnitude (bottom). Flow to east and north is defined positive and flow to west and south negative is defined negative. Note the changing limits of the y-axes. X-axes corresponding to Fig. 3.

3.3 Environmental Conditions

Tide gauge-measured and ADCP pressure-calculated water levels conform to the expected mean water level of 6.5 m with fluctuations of 1-2 m (Fig. 6). Velocity leads water level by 2-3 h (Fig.s 3 and 6), a phase shift the radar captures well. In the north-south component, however, it often fails to capture the change of direction towards the south and mimics it via a decrease in northward velocity magnitude instead (e.g. Fig.s 3 and 6; epochs 8-11 and 71-76). Furthermore, agreement between ADCP and radar results tends to be better during falling tide (Fig.s 3 and 6). In the east-west component, on the other hand, agreement tends to be better during rising tide (Fig.s 3 and 6). During falling tide, most of the bad, overshoot and outlier epochs occur. Yet, the frequency and size of differences between ADCP and radar in such epochs is smaller in the second than in the first half of the experiment. In the north-south component, southward directed currents are correctly indicated more frequently in the second half.

The first half of the experiment is characterized by lower wave height than the second half (Fig. 7). XMFit requires wave crests to be distinguishable from troughs and experience suggests that a significant wave height larger than 0.55 m is needed. The second half of the experiment generally satisfies this criterion very well but a notable decrease in correlation is observed at times of low wave height (e.g. Fig.s 3 and 7; epochs 71-80). In the first half, overshoot and outlier epochs in the east-west component coincide with the epochs of lowest wave height (e.g. Fig.s 3 and 7; epochs 14-19). Furthermore, in the data gap between epochs 47 and 48 output is suppressed because wave heights are so low (0.25-0.55 m) that error metrics of the fitting procedure violate pre-defined boundaries. No correlation between wave period T_{m10} and differences between ADCP and radar can be identified. Yet, the wave period T_{m10} only fluctuates between 3.4 and 5 s during the experiment.

The first half of the experiment is characterized by a lower wind magnitude than the second half (Fig. 8). XMFit requires wind for generation of the surface ripples that make backscattering of radar signals possible. When wind magnitude decreases close to zero, good agreement is still found in the east-west component but not in the north-south component (e.g. Fig.s 3 and 8; epochs 18-21). Epochs of highest wind magnitude coincide with good agreement in both components even though large differences between ADCP and radar are observed for certain epochs, especially in the north-south component (e.g. Fig.s 3 and 8; epochs 51-62 and 79-86). In the east-west component, decreases of the wind component close to zero coincide with mixed agreement and outliers are observed frequently (e.g. Fig.s 3 and 8; epochs 19-33). Epochs of highest east-west wind component magnitude, on the other hand, coincide with good agreement and the less frequent outliers are also smaller (e.g. Fig.s 3 and 8; epochs 51-62 and 82-86). In the north-south component, decreases of the wind component close to zero coincide with varying differences between ADCP and radar (e.g. Fig.s 3 and 8; epochs 5, 9-12, 19-21, 66-70 and 89). Similarly, epochs of highest north-south wind component magnitude coincide with varying differences between ADCP and radar (e.g. Fig.s 3 and 8; epochs 51- 62 and 74-82). Evidently, the increase in wind component magnitude does not have the same benefit in the north-south component. This may be attributed to unknown processes that cause the northward bias, the wind velocity not reaching as high magnitudes in the north-south component as it does in the east-west component or the change of wind direction in the epochs of highest north-south wind component. Whereas wind and current directions are aligned in the epochs of better agreement, they are opposing in the epochs of worse agreement (e.g. Fig.s 3 and 8; epochs 51- 56 compared to 74-82)

4 Conclusions

Remote sensing velocity component estimates from X-band radar were compared to depth-averaged in-situ measurements from an Acoustic Doppler Current Profiler (ADCP) during a field campaign in September 2017 at Ameland inlet. Good agreement was found, and the radar correctly indicated changing flow directions and magnitudes during the tidal cycle. Calculating multiple velocity outputs in the vicinity of the ADCP frame and using their median as the radar result, optimized the agreement between ADCP and radar. Nevertheless, westward outliers of the radar's east-west component and a northward bias of the radar's north-south component were observed. Furthermore, clustering of differences between ADCP and radar showed that certain difference characteristics (e.g. single outliers and overshooting) reappeared frequently throughout the experiment.

Spatial coherence of radar output and error metrics of the fitting procedure were studied as proxies for radar reliability. Fluctuations in spatial coherence and in most error metrics did not correlate well with differences between ADCP and radar. Fluctuations in east-west confidence intervals, on the other hand, coincided with fluctuations in the frequency and the magnitude of outliers. Additionally, environmental conditions were studied as proxies. Water level elevations indicated better agreement in the east-west component during rising tide and better agreement in the north-south component during falling tide (which may be linked to the observed northward bias). Larger waves coincided with better agreement between ADCP and radar, decrease in frequency of radar outliers and smaller confidence intervals. In the east-west component, high wind velocity similarly coincided with better agreement, smaller outlier frequency and smaller confidence intervals. In the north-south component, the benefits of higher wind velocity were smaller. Generally, radar was less prone to faulty outliers when corresponding wind components were directionally aligned and above 5 m/s and waves were high.

Environmental conditions were shown to influence agreement between ADCP and radar. However, only a small number of conditions were assessed and many others were ignored (e.g. precipitation, characteristics of the wave spectrum and residual flows). Likewise, the fitting procedure was assessed only via the most important error metrics. For better gauging of radar reliability (independent of validation data), a quantitative assessment of all their simultaneous influences in conjunction would be necessary. Presently, error metrics already facilitate the suppression of unreasonable outputs. But in this study, their predictive capability did not suffice to always guarantee accurate correspondence to depth-averaged ADCP measurements. Yet, the presented calculation procedure was shown to increase the chances of correspondence with the ADCP. In the end, remote sensing does not aim to match the accuracy of in-situ measurements. Benefits, such as the ability to monitor large areas at high temporal resolution and low cost, can balance the shortcomings in accuracy. As shown in this study, current measurements via X-band MATLAB$^{®}$ Fitting (XMFit) can enable monitoring of currents even in a highly complex region like Ameland inlet.

Acknowledgments

References

Elias, E., 2017. Understanding the present-day morphodynamics of Ameland inlet. Deltares Report for Rijkswaterstaat. Reference 1220339-006-ZKS-0006.

Friedman, J., 2014. Development of an X-band Radar Depth Inversion Model at the Sand Motor. Master Thesis, Delft University of Technology, Available: https://repository.tudelft.nl/islandora/object/uuid%3A2d4773bd-50e5-4507-ae64-1b7c333fb7c1

Gangeskar, R., 2018. Verifying High-Accuracy Ocean Surface Current Measurements by X-Band Radar for Fixed and Moving Installations. IEEE Transactions on Geoscience and Remote Sensing, 56, 4845-4855.

Gawehn, M., Swinkels, C., van Dongeren, A., Hoekstra, R., de Vries, S., Aarninkhof, S.G.J., 2019. A Radar-based depth inversion method to monitor the evolution of nourishments on complex coasts. In prep.

Holman, R., Haller, M.C., 2013. Remote Sensing of the Nearshore. Annual Review of Marine Science, 5, 95-113.

Mueller, D.S., 2015. Velocity bias induced by flow patterns around ADCPs and associated deployment platforms, in: IEEE/OES Eleventh Current, Waves and Turbulence Measurement (CWTM), 2-6 March 2015. 1-7.

Stewart, R.H., Joy, J.W., 1974. HF radio measurements of surface currents.

Deep Sea Research and Oceanographic Abstracts, 21, 1039-1049.

Young, I.R., Rosenthal, W., Ziemer, F., 1985. A three-dimensional analysis of marine radar images for the determination of ocean wave directionality and surface currents.

Journal of Geophysical Research: Oceans, 90, 1049-1059.